---

**Article:**
Zheng, X., Shao, S., Khayyer, A. et al. (3 more authors) (2017) Corrected First-order Derivative ISPH in Water Wave Simulations. Coastal Engineering Journal, 59 (1). 1750010. ISSN 0578-5634

https://doi.org/10.1142/S0578563417500103

---

# Corrected First-order Derivative ISPH in Water Wave Simulations

Xing Zheng[1], Songdong Shao[2,3], Abbas Khayyer[4], Wenyang Duan[1,*], Qingwei Ma[5] and Kangping Liao[1]

[1] College of Shipbuilding Engineering, Harbin Engineering University, Harbin 150001, China

[2] Department of Civil and Structural Engineering, University of Sheffield, Sheffield S1 3JD, UK

[3] School of Water Resources and Electric Power, Qinghai University, Xining 810016, China

[4] Department of Civil and Earth Resources Engineering, Kyoto University, Kyoto 615-8540, Japan

[5] School of Engineering and Mathematical Sciences, City University London, London, EC1V 0HB, UK

* Author of correspondence: duanwenyang@hrbeu.edu.cn

## Abstract

The Smoothed Particle Hydrodynamics (SPH) method is a mesh-less numerical modeling technique. It has been applied in many different research fields in coastal engineering. Due to the drawback of its kernel approximation, however, the accuracy of SPH simulation results still needs to be improved in the prediction of violent wave impact. This paper compares several different forms of correction on the first-order derivative of ISPH formulation aiming to find one optimum kernel approximation. Based on four benchmark case analysis, we explored different kernel corrections and compared their accuracies. Furthermore, we applied them to one solitary wave and two dam-break flows with violent wave impact. The recommended method has been found to achieve much more promising results as compared with experimental data and other numerical approaches.

**Keywords:** ISPH; first-order derivative; kernel correction; wave impact; solitary wave; dam-break flow

## 1. Introduction

The SPH method can well simulate violent water flows and breaking waves, due to its advantageous Lagrangian property. SPH divides the fluid domain into a finite number of mass particles. The movement of particles and the pressure distribution in the fluid are obtained by solving the momentum and continuity equations using the Lagrangian description of the motion. The SPH method was first developed to simulate the evolutions in astrophysics (Lucy, 1977), and was then extended to model free surface flow problems by Monaghan (1994). Because it does not require any mesh in the computational domain, SPH has great potentials to deal with the complex free surface in flows. For example, Colagrossi and Landrini (2003) applied the SPH to two-phase interfacial flows in a dam-break. Souto-Iglesias et al. (2006) studied the violent sloshing at a wide range of rolling frequencies using the SPH. Pu et al. (2013) used the SPH with a Large Eddy Simulation (LES) approach to simulate dam-break flows and compared with results from the Shallow Water Equations (SWEs) model. More benchmark wave breaking and impact SPH applications have been documented by Gomez-Gesteira et al. (2005) and Crespo et al. (2007) and the latest state-of-the-art review in the field can be found in Violeau and Rogers (2016).

With its increasing popularity in different flow applications, some shortcomings of the SPH method emerged, one of which is the low accuracy of kernel approximations which usually cause spurious pressure distributions in wave impact simulation. The numerical noises in pressure could become so large as to distort the underlying physics. As a result, several remedies have been taken such as using higher-order kernel approximations to solve the problem, as documented by Liu et al. (1995) and Ma (2005). These include well-known second-order derivative correction schemes as proposed by Schwaiger (2008), Fatehi and Manzari (2011), Khayyer and Gotoh (2011) and Zheng et al. (2014). However, the accuracy of all these higher-order interpolations is not clear for the discretized kernel form or disordered particle distribution. Besides, the computational expenses could also increase considerably with the interpolation of more variables. Therefore, it seems worthwhile to fully explore the potential of first-order kernel approximations and improve them with robust correction schemes, which is the main aim of present work.

In the previous studies many improvements of the first-order derivative approximations have been introduced. These can be classified into the following three categories: The first improvement was made by the use of an asymmetric form of the pressure gradient or velocity divergence (Monaghan, 1994), but this could not get sufficient accuracy when the neighboring particles become highly disordered. The second one was introduced by using the corrections of kernel gradient (Bonet and

Lok, 1999; Oger et al., 2007), which ensured the SPH pressure gradient term to preserve both linear and angular momentums. However, the tensile instability associated with this formulation introduced tangible errors leading to the clustering of particles (Xu et al., 2009). Thirdly, the Moving Least Square (MLS) principle was adopted for this purpose (Atluri and Shen, 2002; Ma, 2005). The MLS method requires the inversion of matrix and solution of linear algebraic system, so it is very time-consuming when a large number of particles are used in the simulation. Lastly Ma (2008) and Zheng et al. (2014) introduced a Simplified Finite Difference Interpolation (SFDI) approach. This numerical scheme is largely as accurate as the MLS but it does not need the matrix inversion and consumes much less CPU time.

In this study we will comprehensively evaluate the above four correction schemes in the incompressible SPH solver, based on the pressure gradient formulation. After the accuracy analysis on these correction schemes through two patch tests, solitary wave propagation over a constant depth and formation of a standing wave, we will apply the models to three different violent water wave impact cases, in which we fully evaluate the predictions of water surface and impact pressure in comparisons with experimental data documented in the literature. Finally, the optimum correction scheme will be identified. The contribution of present study is, although relevant key formulations were documented by Ma (2005) and Zheng et al. (2014), there have been no extensive comparisons on the accuracy of four different first-order derivative approximations (except for one original formula), or any practical wave impact applications.

The paper is organized as follows: Section 2 presents a review of the ISPH methodology. Section 3 presents the free surface and boundary conditions for the ISPH computation. Section 4 presents all four correction schemes on the first-order derivative (i.e. pressure gradient) calculation. In Section 5, several benchmark numerical tests are carried out to investigate the accuracy and efficiency of various numerical correction schemes as discussed in Section 4, based on the comparisons with analytical solutions. Finally, in the last section the enhanced calculation of water surfaces and impact pressures by the recommended ISPH correction scheme is demonstrated by three application cases. They include the solitary wave slamming on a slope, dam-break flow impact on a vertical wall and dam-break flow overtopping over a trapezoidal structure.

## 2. ISPH Methodology

The fundamental methodology of ISPH can be found in numerous publications, but this is outlined here for the completeness of the work. The method is based on the Lagrangian form of the continuity equation and Navier-Stokes (N-S) momentum equations for the compressible flow, written as

$$\frac{\mathrm{D}\rho}{\mathrm{Dt}} + \rho\nabla\cdot\mathbf{u} = 0 \tag{1}$$

$$\frac{\mathrm{D}\mathbf{u}}{\mathrm{Dt}} = -\frac{1}{\rho}\nabla\mathrm{p} + \mathbf{g} + \nu\nabla^2\mathbf{u} \tag{2}$$

where $\rho$ is the fluid density, $\mathbf{u}$ is the fluid velocity, t is the time, p is the fluid pressure, $\mathbf{g}$ is the gravitational acceleration, and $\nu$ is the kinematic viscosity.

In the incompressible SPH approach, the fluid density is considered as a constant, so the continuity equation is further written as

$$\mathrm{D}\rho/\mathrm{Dt} = 0 \quad \text{or} \quad \nabla\cdot\mathbf{u} = 0 \tag{3}$$

The momentum equation remains the same as Eq. (2).

The computational process of ISPH is composed of two steps: The first step is a prediction, where the velocity field is computed without imposing the incompressibility. The second step is a correction, in which the incompressibility is enforced, with a pressure Poisson equation (PPE) for solving the pressure.

(a) Prediction step

Assuming that the velocities and positions of particles at time t have been found, the values at $\mathrm{t}+\Delta\mathrm{t}$ are predicted by considering the gravitational and viscous terms in Eq. (2) as

$$\mathbf{u}_* = \mathbf{u}_\mathrm{t} + \Delta\mathbf{u}_* \tag{4}$$

$$\Delta\mathbf{u}_* = (\mathbf{g} + \nu\nabla^2\mathbf{u})\Delta\mathrm{t} \tag{5}$$

$$\mathbf{r}_* = \mathbf{r}_\mathrm{t} + \mathbf{u}_*\Delta\mathrm{t} \tag{6}$$

where $\mathbf{u}_\mathrm{t}$ and $\mathbf{r}_\mathrm{t}$ are the velocity and position, respectively, at time t. $\Delta\mathrm{t}$ is the time step, and $\mathbf{u}_*$ and $\mathbf{r}_*$ are the intermediate velocity and position of the particles.

(b) Correction step

The velocity update in the correction step is by

$$\Delta\mathbf{u}_{**} = -\frac{\Delta\mathrm{t}}{\rho}\nabla\mathrm{p}_{\mathrm{t}+\Delta\mathrm{t}} \tag{7}$$

where $p_{t+\Delta t}$ is the pressure at $t+\Delta t$. So the velocity and position of particles at $t+\Delta t$ are given by

$$\mathbf{u}_{t+\Delta t} = \mathbf{u}_{*} + \Delta \mathbf{u}_{**} \tag{8}$$

$$\mathbf{r}_{t+\Delta t} = \mathbf{r}_{t} + \frac{\mathbf{u}_{t} + \mathbf{u}_{t+\Delta t}}{2}\Delta t \tag{9}$$

Combining Eq. (8) with Eq. (3), the following PPE is obtained as

$$\nabla^2 p_{t+\Delta t} = \frac{\rho \nabla \cdot \mathbf{u}_{*}}{\Delta t} \tag{10}$$

Similarly, Gui et al. (2014) proposed a projection-based incompressible method by imposing density invariance on Eq. (10), which leads to the equation below

$$\nabla \cdot (\frac{1}{\rho^{*}} \nabla p_{t+\Delta t}) = \frac{\rho - \rho^{*}}{\rho \Delta t^2} \tag{11}$$

where $\rho^{*}$ is the particle density at the intermediate time step and is calculated by $\rho^{*} = \sum_{j=1}^{N} m_j W_{ij}$, where $m$ is the particle mass and $W$ is the SPH kernel function. For the incompressible fluid, the intermediate density is only slightly different from the original density. As indicated by Hu and Adams (2007), Eqs. (10) and (11) are essentially equivalent and thus they suggested to solve the two incompressibility equations simultaneously, in which the solution of density invariant equation (Eq. (11)) was used to adjust the position of particles while the solution of velocity-divergence-free equation (Eq. (10)) was used to adjust their velocities.

By combining the merits of both, Zhang et al. (2006) proposed the following mixed PPE formulation as

$$\nabla^2 p_{t+\Delta t} = \gamma \frac{\rho - \rho^{*}}{\Delta t^2} + (1-\gamma)\frac{\rho \nabla \cdot \mathbf{u}_{*}}{\Delta t} \tag{12}$$

The above equation was also used by Ma and Zhou (2009) in their MLPG_R method, where $\gamma$ is an artificial coefficient and in the range of 0 ~ 1. According to Zhang et al. (2006), the numerical predictions on violent water wave impact seem to be most satisfactory if $\gamma$ is specified a properly small value. On the other hand, in order to achieve accurate results without the need of using density term (i.e. $\gamma$ = 0), the position of particles should be shifted at each time step in a way similar to the re-meshing or dynamic re-gridding, such as based on the Fick's law (Lind et al., 2012). In this paper, a fixed value of $\gamma$ = 0.01 is simply used based on our previous computational experiences. More detailed study on this coefficient in different flow applications can be found in Gui et al. (2014).

For solving the pressure Poisson equation (Eq. (10), (11) or (12)), the often employed SPH scheme is

$$\nabla^2 p_i \approx \sum_{j=1}^{N} 2\frac{m_j}{\rho_j}\frac{(\mathbf{r}_{ij})_\alpha W(\mathbf{r}_{ij})_\alpha}{\mathbf{r}_{ij}^2+\delta^2} p_{ij} \tag{13}$$

where $p_{ij} = p_i - p_j$ and $\mathbf{r}_{ij} = \mathbf{r}_i - \mathbf{r}_j$, subscript α denotes the spatial directions, which correspond to x and y in 2D. $W(\mathbf{r}_{ij})_\alpha$ is the partial derivative of kernel function with respect to coordinate α direction, $(\mathbf{r}_{ij})_\alpha$ is the component of vector $\mathbf{r}_{ij}$, and $(\mathbf{r}_{ij})_\alpha W(\mathbf{r}_{ij})_\alpha$ is calculated by $\mathbf{r}_{ij}\cdot\nabla W(\mathbf{r}_{ij})$. $\delta$ is a small value to prevent singularity of the denominator.

Here it should be pointed out that in the current SPH application field, the accuracy of the method is influenced by quite a few complex factors, some of which are still under intensive debate. Turbulence is one of these issues and its influence also varies depending on the situations. In this study the turbulence was not taken into consideration by adding the sub-particle-scale (SPS) turbulence model, since our primary goal is to evaluate different correction schemes. Besides, in our numerical simulations, the effect of SPS turbulence on the macroscopic behavior of hydrodynamics, such as the water surface and impact pressure, etc seems to be relatively small due to the use of refined particle size. However, when coarser particles are used in more practical engineering domain, the SPS turbulence could become quite significant and thus the explicit turbulence model should be considered. Non-turbulence modeling in wave breaking and impact has also been reported by Khayyer et al. (2008) and Jian et al. (2016).

## 3. Free Surface and Boundary Conditions

### 3.1 Free surface boundary

The condition on the free surface is very simple in the SPH, which states that the pressure of water on its free surface is equal to the atmospheric pressure, i.e.

$$p = 0 \tag{14}$$

In the Weakly Compressible SPH (WCSPH) method, this condition can be automatically satisfied, as long as the density on the free surface is estimated correctly. However, for the ISPH approach the free surface particles have to be identified. The pressure value on the free surface particles is then used as Dirichlet boundary condition to solve the Pressure Poisson equation. In this paper, the identification of

free surface particles is achieved through the local density and additional three auxiliary functions (Zheng et al., 2014).

### 3.2 Solid wall boundary

On the impermeable solid wall, the following condition should be satisfied

$$\mathbf{u}\cdot\mathbf{n}=\mathbf{U}\cdot\mathbf{n} \tag{15}$$

and

$$\mathbf{n}\cdot\nabla \mathrm{p}=\rho\left(\mathbf{n}\cdot\mathbf{g}-\mathbf{n}\cdot\dot{\mathbf{U}}+\nu\,\mathbf{n}\cdot\nabla^2\mathbf{u}\right) \tag{16}$$

where $\mathbf{n}$ is the unit vector that is normal to the solid boundary, $\mathbf{U}$ and $\dot{\mathbf{U}}$ are the velocity and acceleration of the solid boundary, respectively. It is noted that the traditional WCSPH does not need the condition specified by Eq. (16), as it does not solve the boundary value problem for the pressure. In ISPH model, however, the condition in Eq. (16) should be necessary. It is obvious that one must compute the term $\nabla^2\mathbf{u}$ when using Eq. (16), in which a second-order derivative on the solid boundary is required. To avoid this, Ma and Zhou (2009) combined Eqs. (4) and (16) and proposed an alternative form of the equation and this is used here

$$\mathbf{n}\cdot\nabla \mathrm{p}=\frac{\rho}{\Delta \mathrm{t}}\mathbf{n}\cdot(\mathbf{u}^{*}-\mathbf{U}) \tag{17}$$

Numerical implementation of Eq. (15) is quite straightforward, i.e., the normal velocity of fluid particles is imposed to be equal to that of the wall.

Besides, the pressure condition on the solid boundary is described by the following set of equations. One distinct feature is that the normal pressure gradient is computed at the boundaries without the need of using ghost particles. This could significantly improve the simulation accuracy near the solid walls and meanwhile, effectively reduce the computational cost

$$\left.\frac{\partial \mathrm{p}}{\partial \mathrm{x}}\right|_{\mathrm{i}}=\sum_{\mathrm{j}=1,\,\mathrm{j}\neq\mathrm{i}}^{\mathrm{N}}\frac{\mathrm{n}_{\mathrm{i,y}}\mathrm{B}_{\mathrm{ij,x}}-\bar{\mathrm{n}}_{\mathrm{i,xy}}\mathrm{B}_{\mathrm{ij,y}}}{\mathrm{n}_{\mathrm{i,x}}\mathrm{n}_{\mathrm{i,y}}-\bar{\mathrm{n}}_{\mathrm{i,xy}}{}^{2}}(\mathrm{p}_{\mathrm{j}}-\mathrm{p}_{\mathrm{i}}) \tag{18}$$

$$\left.\frac{\partial \mathrm{p}}{\partial \mathrm{y}}\right|_{\mathrm{i}}=\sum_{\mathrm{j}=1,\,\mathrm{j}\neq\mathrm{i}}^{\mathrm{N}}\frac{\mathrm{n}_{\mathrm{i,x}}\mathrm{B}_{\mathrm{ij,y}}-\bar{\mathrm{n}}_{\mathrm{i,xy}}\mathrm{B}_{\mathrm{ij,x}}}{\mathrm{n}_{\mathrm{i,x}}\mathrm{n}_{\mathrm{i,y}}-\bar{\mathrm{n}}_{\mathrm{i,xy}}{}^{2}}(\mathrm{p}_{\mathrm{j}}-\mathrm{p}_{\mathrm{i}}) \tag{19}$$

where

$$\mathrm{n}_{\mathrm{i},\mathrm{x}_{\mathrm{m}}}=\sum_{\mathrm{j}=1,\,\mathrm{j}\neq\mathrm{i}}^{\mathrm{N}}\frac{\left(\mathrm{r}_{\mathrm{j},\mathrm{x}_{\mathrm{m}}}-\mathrm{r}_{\mathrm{i},\mathrm{x}_{\mathrm{m}}}\right)^{2}}{\left|\mathbf{r}_{\mathrm{j}}-\mathbf{r}_{\mathrm{i}}\right|^{2}}\mathrm{W}\left(\left|\mathbf{r}_{\mathrm{j}}-\mathbf{r}_{\mathrm{i}}\right|\right)\qquad(\mathrm{m}=1\text{ or }2) \tag{20}$$

$$\bar{\mathrm{n}}_{\mathrm{i,xy}}=\sum_{\mathrm{j}=1,\,\mathrm{j}\neq\mathrm{i}}^{\mathrm{N}}\frac{\left(\mathrm{r}_{\mathrm{j},\mathrm{x}_{\mathrm{m}}}-\mathrm{r}_{\mathrm{i},\mathrm{x}_{\mathrm{m}}}\right)\left(\mathrm{r}_{\mathrm{j},\mathrm{x}_{\mathrm{k}}}-\mathrm{r}_{\mathrm{i},\mathrm{x}_{\mathrm{k}}}\right)}{\left|\mathbf{r}_{\mathrm{j}}-\mathbf{r}_{\mathrm{i}}\right|^{2}}\mathrm{W}\left(\left|\mathbf{r}_{\mathrm{j}}-\mathbf{r}_{\mathrm{i}}\right|\right)\quad(\mathrm{m}=1\text{ or }2;\ \mathrm{k}=1\text{ or }2,\ \mathrm{m}\neq\mathrm{k}) \tag{21}$$

$$B_{ij,x_m} = \frac{\left(r_{j,x_m} - r_{i,x_m}\right)}{\left|\mathbf{r}_j - \mathbf{r}_i\right|^2} W\left(\left|\mathbf{r}_j - \mathbf{r}_i\right|\right) \tag{22}$$

More details on the solid boundary discretization scheme can refer to Ma and Zhou (2009). It should be mentioned here that all the numerical results in the paper have been obtained with these improved solid boundary treatments. The difference only lies in the use of different first-order derivative calculations for the inner particles. Thus all of the following correction models are compared on an equal basis.

## 4. Correction Schemes on First-order Derivative

In this section, we will fully review and compare four commonly used SPH formulations on the first-order derivative, e.g. the pressure gradient.

Two important SPH representations of first-order derivative term are the pressure gradient and velocity divergence, respectively, as

$$\nabla p_i = \rho_i \sum_{j=1}^{N} m_j \left(\frac{p_j}{\rho_j^2} + \frac{p_i}{\rho_i^2}\right) \nabla_i W(\mathbf{r}_{ij}) \tag{23}$$

$$\nabla \cdot \mathbf{u}_i = -\frac{1}{\rho_i} \sum_{j=1}^{N} m_j \mathbf{u}_{ij} \cdot \nabla_i W(\mathbf{r}_{ij}) \tag{24}$$

where $\mathbf{u}_{ij} = \mathbf{u}_i - \mathbf{u}_j$. In this paper, the kernel is based on a cubic spline function which has been widely used in SPH hydrodynamics. In previous SPH works, most of the improved first-order derivative computations were documented on the pressure gradient and this practice is also followed here.

### 4.1 Anti-symmetric form

This is the earliest formulation used in SPH free surface flows and is still widely accepted today due to its simplicity and effectiveness

$$-\frac{\nabla p_{i,\alpha}}{\rho_0} = -\sum_{j=1}^{N} \left(\frac{p_i}{\rho_i^2} + \frac{p_j}{\rho_j^2}\right) W_{ij,\alpha} \tag{25}$$

Since originally proposed by Monaghan (1994), Eq. (25) has been successfully used in incompressible SPH solvers as well with promising result in coastal hydrodynamics. However, it was later found that this formulation can only guarantee the linear momentum conservation but the angular momentum is not conserved. As a result, it has significant weakness when applied to the breaking waves, in which the collapse and coalescence of free surfaces cannot be clearly illustrated.

4.2 Kernel correction form

To address the drawback of Eq. (25), Khayyer et al. (2008) proposed a corrected kernel formulation of the pressure gradient from Bonet and Lok (1999) as follows

$$-\frac{\nabla p_{i,\alpha}}{\rho_0} = -\frac{1}{\rho_0}\sum_{j=1}^{N}\frac{m_j}{\rho_j}(p_j - p_i)L^{\alpha\beta}W_{ij,\beta} \tag{26}$$

$$L^{\alpha\beta} = \left[\sum_{j=1}^{N}(r_{j,\alpha} - r_{i,\alpha})W_{ij,\beta}\right]^{-1} \tag{27}$$

The above two equations improved the SPH simulation accuracy and were increasingly adopted in subsequent SPH applications. However, as pointed out by Xu et al. (2009), although the accuracy of first-order derivative has been improved by using Eqs. (26) and (27), they could generate tensile instability on the neighboring particles and this might influence the practical model applications.

4.3 Mixed symmetric kernel gradient correction form

To further improve the accuracy and stability of SPH method, the mixed symmetric correction of kernel gradient, which was based on the concept of symmetric SPH by Zhang and Batra (2009), has been proposed by Xu and Deng (2016) for the study of viscous and viscoelastic flows. The method is referred as mixed and symmetric, since it combines the advantages of traditional and symmetric SPHs, which takes the following form

$$-\frac{\nabla p_{i,\alpha}}{\rho_0} = -\frac{1}{\rho_0}\sum_{j=1}^{N}\frac{m_j}{\rho_j}(p_j - p_i)L^{\alpha\beta}(r_{j,\beta} - r_{i,\beta})W_{ij} \tag{28}$$

where $L^{\alpha\beta} = \left[\sum_{j=1}^{N}(r_{j,\alpha} - r_{i,\alpha})(r_{j,\beta} - r_{i,\beta})W_{ij}\right]^{-1}$ is an inverse matrix.

Here it should be noted that the above mixed and symmetric approach requires the inversion of matrix, which might be singular for highly irregular particle distributions. The good point is that the matrix $L^{\alpha\beta}$ in Eq. (28) is symmetric with a reduced storage requirement. Also, because there are no kernel derivatives involved, it can allow for a wide range of kernel functions and improve the stability of computation to avoid the tensile instability issue.

4.4 Simplified Finite Difference Interpolation (SFDI) form

During the inverse matrix calculations in Eq. (26) and (28), the ill-conditioned matrixes can be generated when the particles are close to the free surface or there is only one single particle in the simulation system. To solve this problem, Ma (2008) and Zheng et al. (2014) introduced a simplified Finite Difference Interpolation (SFDI)

method for the first-order derivative calculation. This method arises from the Taylor series expansion by multiplying it with a weight derivative $\frac{(r_{j,\alpha}-r_{i,\alpha})}{|r_j-r_i|^2}W_{ij}$ to both sides of the pressure gradient equation. In summary, the gradient of pressure $p_i$ in a two-dimensional space can be approximated by the following set of equations as

$$-\frac{\nabla p_{i,\alpha}}{\rho_0}=-\frac{1}{\rho_0}\frac{C_{i,\alpha}-a_{i,\alpha k}C_{i,k}}{1-a_{i,\alpha k}a_{i,k\alpha}} \tag{29}$$

$$C_{i,\alpha}=\frac{1}{n_{i,\alpha}}\sum_{j=1,j\neq i}^{N}(p_j-p_i)\frac{(r_{j,\alpha}-r_{i,\alpha})}{|r_j-r_i|^2}W_{ij} \tag{30}$$

$$a_{i,\alpha k}=\frac{1}{n_{i,\alpha}}\sum_{j=1,j\neq i}^{N}\frac{(r_{j,\alpha}-r_{i,\alpha})(r_{j,k}-r_{i,k})}{|r_j-r_i|^2}W_{ij} \tag{31}$$

$$n_{i,\alpha}=\sum_{j=1,j\neq i}^{N}\frac{(r_{j,\alpha}-r_{i,\alpha})^2}{|r_j-r_i|^2}W_{ij} \tag{32}$$

where N is the number of neighbouring particles affecting particle i, $\alpha$ = 1 or 2, k = 1 or 2, $\alpha\neq k$, $r_{j,\alpha}$ or $r_{j,k}$ is the component of position vector in x or y direction, respectively. More detailed mathematical derivations can be refereed to Ma (2008). As Eq. (29) does not involve the inverse matrix calculation, it can avoid the occurrence of ill-conditioned matrix. Furthermore, following the accuracy analysis carried out by Ma (2008) and Zheng et al. (2014), the error of this method is very close to that in the Moving Least Square (MLS) method, but the CPU expenses are much lower. Here it should be noted that our simplified SFDI is actually another kind of kernel approximation method for the first-order derivative calculation, but not related to either conventional FDM or Generalized FDM.

## 5. Numerical Test on Different Correction Schemes

Before investigating the accuracy of different SPH first-order derivative schemes, we make the following classifications:

(1) ISPH - standard incompressible SPH formulation based on Eq. (25);

(2) CISPH1 - incompressible SPH based on kernel correction Eq. (26);

(3) CISPH2 - incompressible SPH based on mixed/symmetric kernel gradient correction Eq. (28);

(4) CISPH3 - incompressible SPH based on Simplified Finite Difference Interpolation Eq. (29).

## 5.1 Analytical patch test

Although Bonet and Lok (1999) and Ma (2008) initiated benchmark patch tests to estimate the first-order derivative of analytical functions on a set of randomly distributed particles, more detailed studies will be carried out in this section to compare the performance of ISPH, CISPH1, CISPH2 and CISPH3.

For such a purpose, we consider a function of $f(x, y) = x^2 + y^2$. The spatial domain is chosen as a square with the side length of 1 within $0 \le x \le 1$ and $0 \le y \le 1$. The domain is first divided into a series of small square elements (using $\Delta x \times \Delta y$ with $\Delta x = \Delta y = s$). Then the particles are redistributed by $\Delta x' = \Delta y' = s[1 + k(R_n - 0.5)]$, where $R_n$ is a random number between 0 and 1, and $k$ is a constant. $k = 0$ leads to a regular particle distribution, which is shown in Fig. 1 (a) with particle number $N = 900$. $k > 0$ corresponds to a disordered particle distribution and Fig. 1 (b) illustrates the situation when $k = 0.2$ with the same particle number.

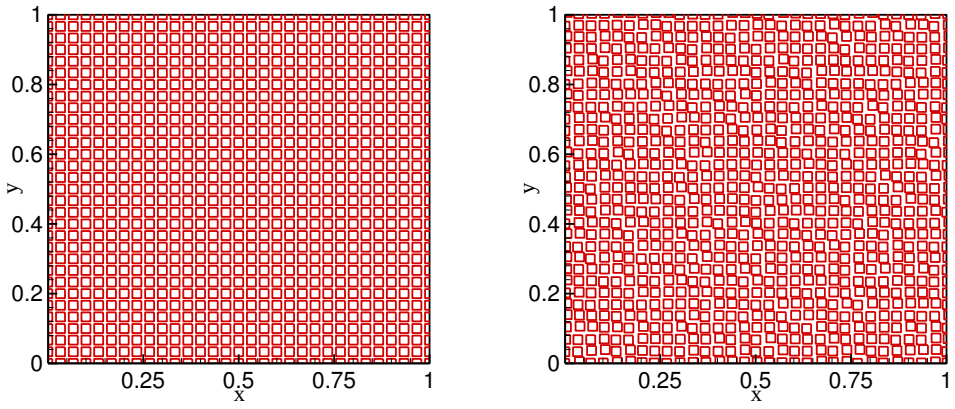


Fig. 1 Particle distributions within a square domain with particle number $N = 900$. (a) $k = 0$ for a uniform distribution; (b) $k = 0.2$ for a disordered distribution.

The first-order derivative of $f(x, y) = x^2 + y^2$, $\nabla f$, is calculated directly by taking its analytical derivative denoted as $\nabla f_{i,a}$. This will also be computed numerically by using our four SPH first-order formulations as mentioned above, which is denoted by $\nabla f_{i,c}$. The averaged error between the analytical and numerical approaches are quantified by

$$Er = \frac{1}{N}\sqrt{\sum_{i=1}^{N}(\nabla f_{i,c} - \nabla f_{i,a})^2} \qquad (33)$$

The test cases with different particle numbers of N = 900, 1600, 3600, 6400 and 10000, are considered. The results are presented in Figs. 2 and 3, respectively, for the uniform and random particle configurations.

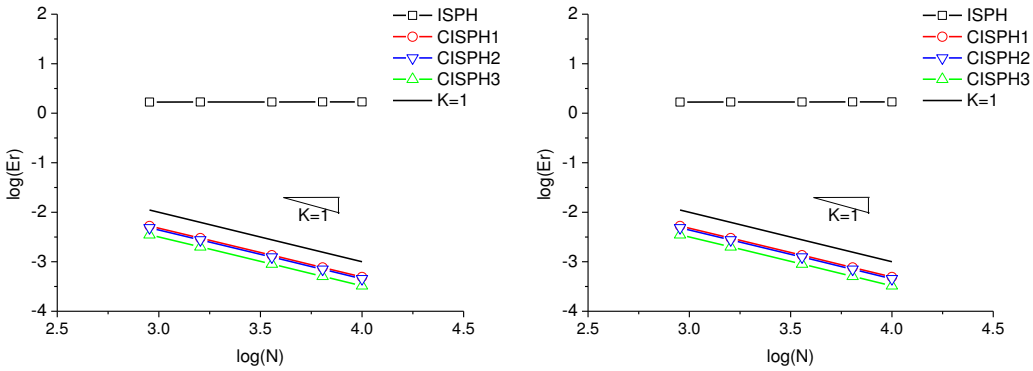


Fig. 2 Errors for different first-order derivative schemes under uniform particle distributions: (a) x - component error; (b) y - component error.

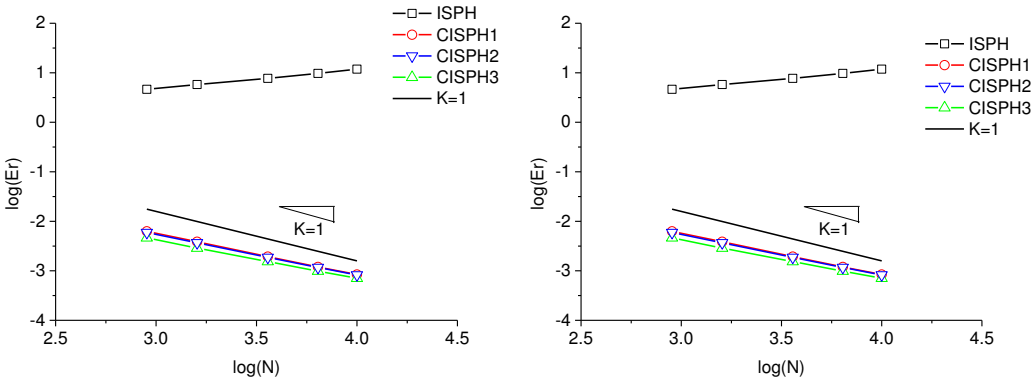


Fig. 3 Errors for different first-order derivative schemes under disordered particle distributions: (a) x - component error; (b) y - component error.

Fig. 2 shows the average errors calculated by Eq. (33) for different values of N under k = 0. It shows that when the particles are uniformly distributed, the error computed by using the standard ISPH formulation keeps nearly constant. In comparison, the errors computed by CISPH1, CISPH2 and CISPH3 unanimously demonstrate a deceasing trend with the increasing particle number. Besides, the slopes of error curves correlating logarithmic Er and N approach unity, which suggests that their numerical accuracies are close to the first-order. Besides, the comparisons among different error lines clearly indicate that CISPH3 based on Eq. (29) can achieve the

highest accuracy leading to the minimum errors across a range of particle sizes. Fig. 2 (a) and (b) showed the two components of first-order derivative error in x and y directions, respectively, and both demonstrated the same trend.

On the other hand, when the particles become highly disordered, Fig. 3 shows that the averaged error computed by standard ISPH Eq. (25) surprisingly increase with an increase in the particle numbers. This implies that higher particle resolution alone is not sufficient to achieve a converged solution. In contrast, the computational results of CISPH1, CISPH2 and CISPH3 can still maintain the first-order accuracy even under irregular particle configurations. Again, CISPH3 which is based on Eq. (29), achieved the highest accuracy as compared with other correction schemes.

One common feature found in both Fig. 2 and 3 is that the numerical errors decrease with the increasing particle numbers, which shows the convergence of the model based on modified Equations (26), (28) and (29). Another feature is that Eqs. (26) and (28) have very similar accuracy and convergence behaviors while Eq. (29) clearly improved these.

Moreover, we investigated another test function f(x,y) = exp (2x+ 3y), which is much more complex than the original one due to its highly non-linear property. The error and convergence behaviors are found to be almost the same as those from the previous test function. The relevant figures corresponding to Figs. 2 and 3 are shown in Figs. 4 and 5.

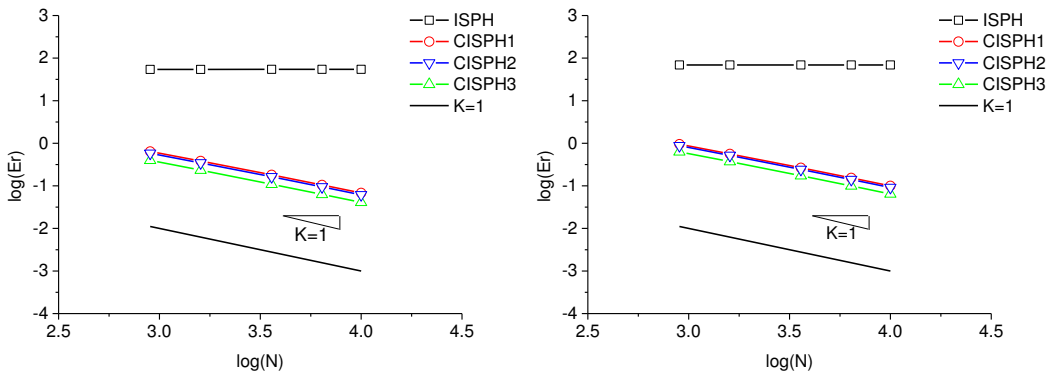


Fig. 4 Errors for different first-order derivative schemes under uniform particle distributions for $f(x, y) = e^{2x+3y}$: (a) x - component error; (b) y - component error.

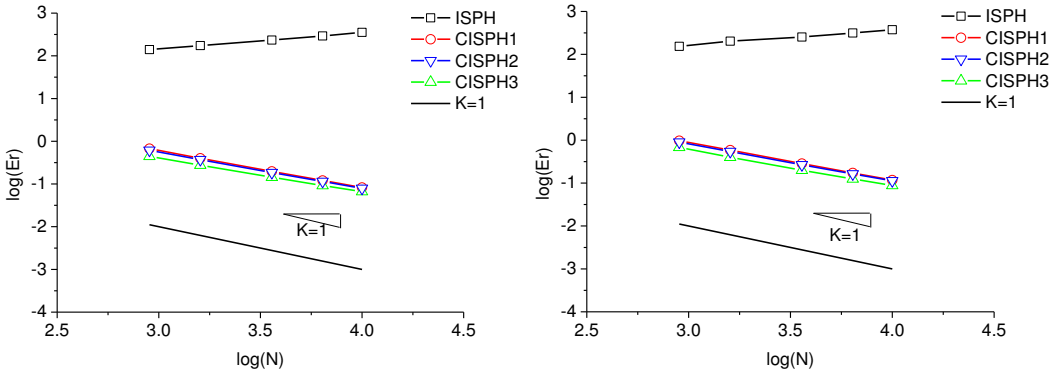


Fig. 5 Errors for different first-order derivative schemes under disordered particle distributions for $f(x, y) = e^{2x+3y}$: (a) x - component error; (b) y - component error.

## 5.2 Solitary wave propagation on a constant depth

As a further test on different numerical schemes for the first-order derivative corrections, the solitary wave propagation on a constant water depth is considered. The interaction between tsunami waves and coastal structures is the topic related to many coastal and ocean engineering problems and has attracted increasing attentions. In most cases, the solitary wave is used to represent certain characteristics of the tsunami wave (Jian et al., 2011). To verify the numerical results, the computed solitary wave profiles by the SPH will be compared with the analytical solution derived from the Boussinesq equation, which is represented as

$$\eta(x,t) = a\,\mathrm{sech}^2\left[\sqrt{\frac{3a}{4d^3}}(x-ct)\right] \tag{34}$$

where $\eta$ is the water surface elevation, $a$ is the wave amplitude, $d$ is the constant water depth and $c = \sqrt{g(d+a)}$ is the solitary wave celerity.

We consider a wave amplitude $a$ = 0.05 m, water depth $d$ = 0.25 m and total length of the tank $l$ = 10.0 m. Fig. 6 shows the computed free surface profiles with the analytical one for the different ISPH methods, at time $t$ = 5.0 s and for the vertical particle number in the water depth $N_y$ = 30. The computational time step is $\Delta t$ = 0.001 s. The solitary wave was generated by a piston wave maker. It shows that the wave surface profile computed by CISPH3 of Eq. (29) achieved the best agreement with the analytical solution as compared with other three ISPH methods. Especially the original ISPH significantly under-predicted the solitary wave height. It is obvious that the accuracy of first-order derivative of pressure gradient (i.e. pressure gradient) can greatly influence the computed wave height.

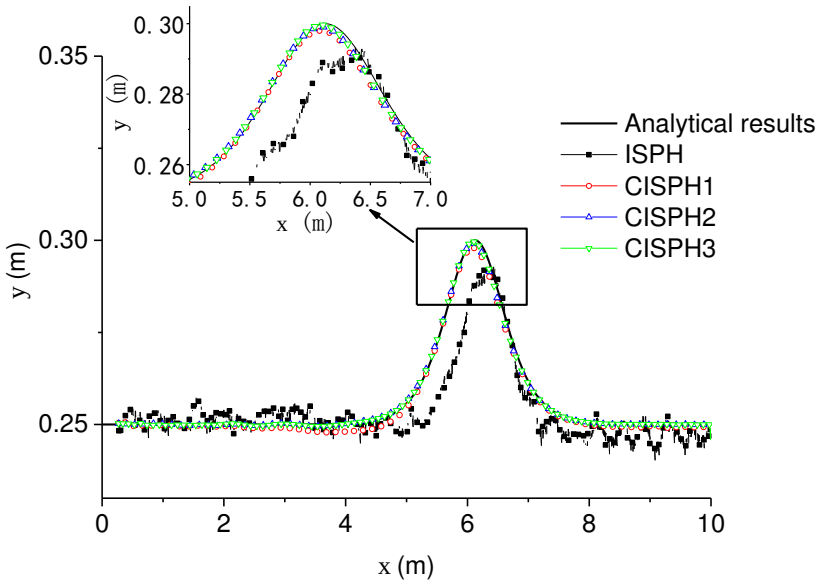


Fig. 6 Free surface comparisons between analytical and different ISPH correction schemes for solitary wave propagation when $t$ = 5.0 s and $N_y$ = 30.

To shed quantitative insight into the numerical errors, Fig. 7 gives the convergence tests on free surface elevation with different particle numbers and various ISPH correction schemes as represented by Eqs. (25), (26), (28) and (29), at time $t$ = 5 s. The error of free surface elevations is defined as

$$\mathrm{Err} = \sqrt{\sum_{i=1}^{Ntf}(\eta_{a,i} - \eta_{c,i})^2} \Big/ \sum_{i=1}^{Ntf}\eta_{a,i} \tag{35}$$

where $\eta_{a,i}$ is the analytical wave surface elevation, $\eta_{c,i}$ is the numerical one, and Ntf is the total number of particles that stay on the free surface. According to Fig. 7, all four ISPH methods showed convergence behavior with an increase in the particle numbers. Among them CISPH3 result has the steepest slope of the error line, which indicates it is the most accurate first-order derivative scheme. Besides, the trend of all error lines in Fig. 7 is consistent with the wave surface profiles as shown in Fig. 6. That is to say, CISPH3 achieved the best performance, followed by CISPH2 and CISPH1. In comparison, the standard ISPH pressure gradient formulation as represented by Eq. (25) is least accurate.

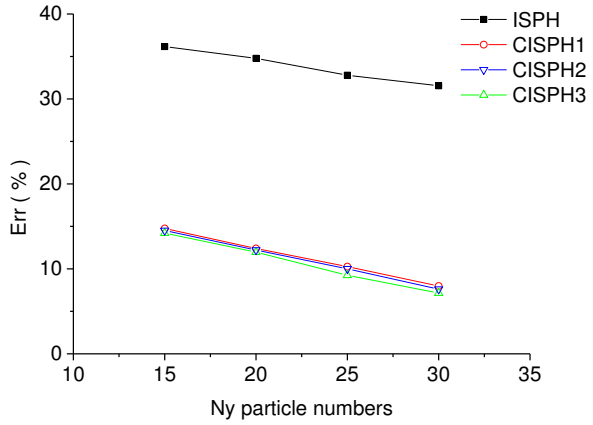


Fig. 7 Convergence test on wave surface errors by using different ISPH methods with different vertical particle numbers $N_y$.

To show the wave evolution pattern under different particle resolutions, Fig. 8 gives the comparisons of wave surface profile computed by SPH using different $N_y$ values, with the analytical solution at several time instants. Here we just present the results of CISPH3 computation. It shows that the numerical wave surfaces approach to the analytical one with the increasing particle number in vertical direction. Both the wave height and wave shape are well maintained during the wave propagation.

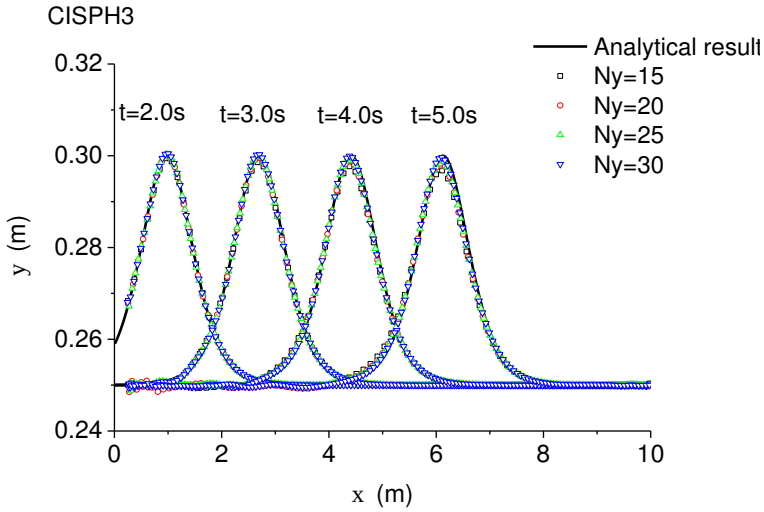


Fig. 8 Comparisons of wave surface profile computed by CISPH3 using different $N_y$ values with analytical solution.

## 5.3 Standing wave generation

The modeling system of standing wave is shown in Fig. 9, where the reference level ox is located on the still water surface and vertical axis oy is pointing upwards. The considered water depth is d = 1.0 m and tank length l = 2.0 m.

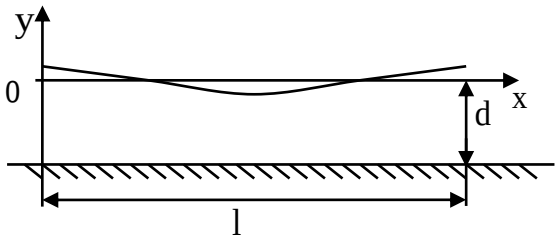


Fig. 9 Modeling system of standing wave.

When the wave amplitude is small, liner wave theory is accurate enough to obtain the analytical solution of the standing wave model (Zou, 2005). The analytical wave surface profile is represented as

$$\eta = a\cos kx\sin \omega t \tag{36}$$

where a is the wave amplitude, k is the wave number, $\omega$ is the angular frequency, and $\omega^2 = gk\tanh(kd)$. The velocities of water particles under a standing wave can be analytically represented by

$$u = \varphi_x = -\frac{a\omega}{\sinh kd}\cos \omega t[\cosh k(y+d)\sin kx] \tag{37}$$

$$v = \varphi_y = \frac{a\omega}{\sinh kd}\cos \omega t[\sinh k(y+d)\cos kx] \tag{38}$$

In the numerical test we assumed a = 0.025 m and $\omega$ = 1.769 $s^{-1}$. Four different particle numbers of 3200, 7200, 12800 and 20000 were used, corresponding to vertical particle number of $N_y$ = 40, 60, 80 and 100, respectively. The computational time step is fixed at $\Delta t$ = 0.001 s. The initial setup of SPH particle system is shown in Fig. 10, in which they are assigned the analytical wave profiles and 2D velocities based on the above equations. The computed time histories of wave surface profile at the center of tank x = 1.0 m are shown in Fig. 11. Four different ISPH results and analytical solution are given for a comparison, which again shows the superiority of CISPH3 computation.

Finally, following Eq. (35) we provided the convergence test on wave surface errors for different ISPH methods with different vertical particle numbers $N_y$ as shown in

Fig. 12. It shows CISPH3 is the most accurate one and also the numerical errors decrease with the increasing particle number for all four methods. The data are extracted at location x = 1.0 m and at simulation time t = 9 s.

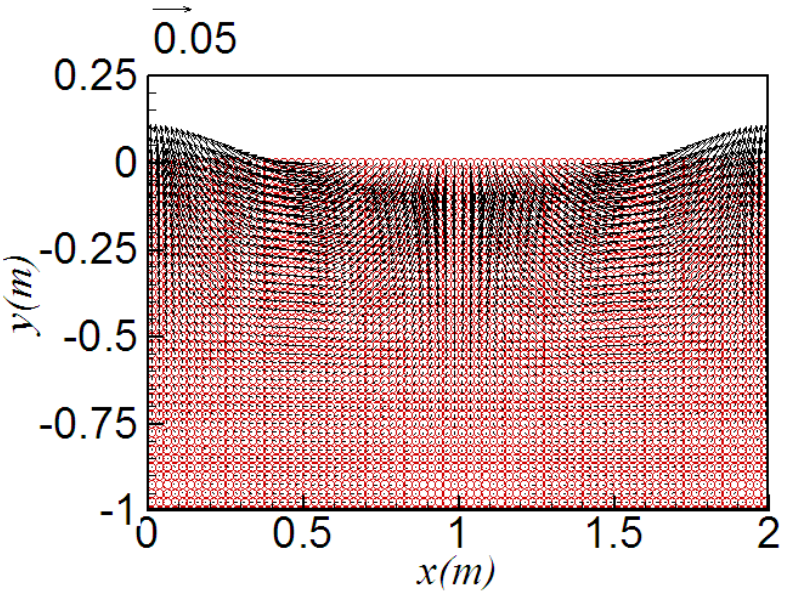


Fig. 10 Initial particle profile and velocity distributions of standing wave system.

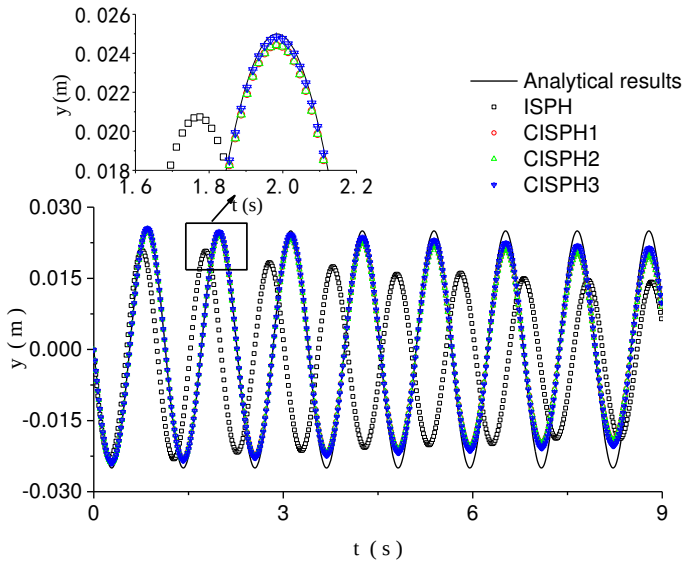


Fig. 11 Time histories of wave surface profile computed by different ISPH methods and analytical solution.

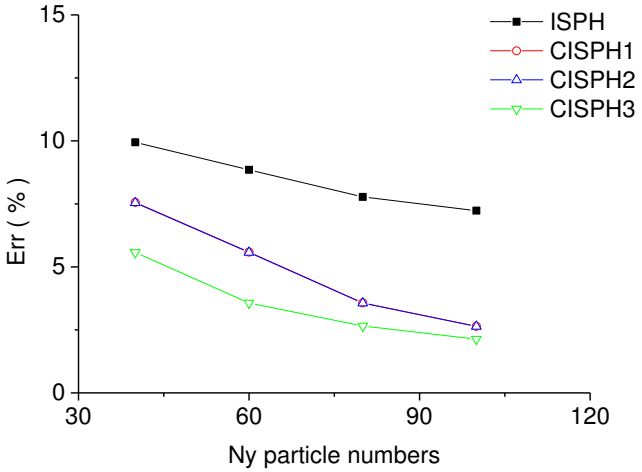


Fig. 12 Convergence test on wave surface errors by using different ISPH methods with different vertical particle numbers $N_y$.

## 6. Model Applications in Violent Wave Impact

In this section, we will use the proposed CISPH3 method as shown in Eq. (29) to study three practical wave impact problems: the solitary wave impact on a slope and two dam-break flow interactions with the structure, by examining the water surface profile and flow impact pressure. The numerical results will be validated against the documented experimental data. The robustness of CISPH3 correction scheme will be demonstrated through comparisons with the others using practical model applications.

### 6.1 Solitary wave impact on a slope

In order to justify the improvement of impact pressure computation of a solitary wave during its interaction with a slope, Fig. 13 illustrates the model of a wave tank. The numerical settings are based on the physical experiment carried out at Harbin Engineering University, China. The constant water depth and total length of the tank are the same as those given in Section 5, i.e. $d$ = 0.25 m and $l$ = 10.0 m, except with a larger incident wave amplitude $a$ = 0.15 m. In this setting, there is an added slope on the right-hand side of the flume with an inclination angle $\alpha$ = 60°. A pressure sensor $p_1$ is located on the slope surface at a distance of $h_1$ = 0.05 m from the bottom. The total vertical height of the slope is $h$ = 1.0 m. All ISPH computations are carried out with a particle spacing dx = 0.008 m and time step $\Delta t$ = 0.001 s, including the original ISPH and three corrected CISPHs.

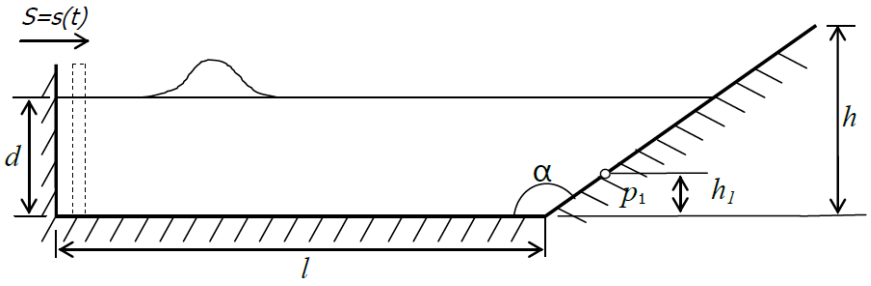


Fig. 13 Numerical wave tank for solitary wave impact on a slope.

From our most promising CISPH3 computations, Fig. 14 shows the solitary wave profile and pressure contours at different times during its propagation and run-up, and Fig. 15 (a) – (d) is the enlarged figure showing the coastal wave process such as its running-up, running-down and overturning. In these figures, the value of pressures has been normalized by the height of slope, i.e. $\rho gh$ . Fig. 14 shows the solitary wave propagating stably in a constant depth with little variation in the wave height and wave shape. The pressures under the wave follow hydrostatic law with almost no numerical noise. This is a strong indication of the improved ISPH numerical scheme in the pressure calculations. From Figure 15, the near-shore solitary wave process can be divided into four distinct stages: First the wave approaches the shoreline and starts to run up along the slope, and the wave front is elevated as shown in Fig. 15 (a); Second when the wave front reaches the highest climbing point of the slope, it starts to run down as shown in Fig. 15 (b); Then as shown in Fig. 15 (c) when the wave reaches the maximum run-down point, there appears a wave over-overturning feature evidenced by a backwash. At this moment, the local pressures under the wave exceed the hydrostatic value due to the additional vertical acceleration of the fluid particles. Finally, after the wave has fully retreated it restarts to run up against the slope again, but with a much smaller intensity. As a result, the maximum run-up point as shown in Fig. 15 (d) is significantly lower than the first run-up point in Fig. 15 (b).

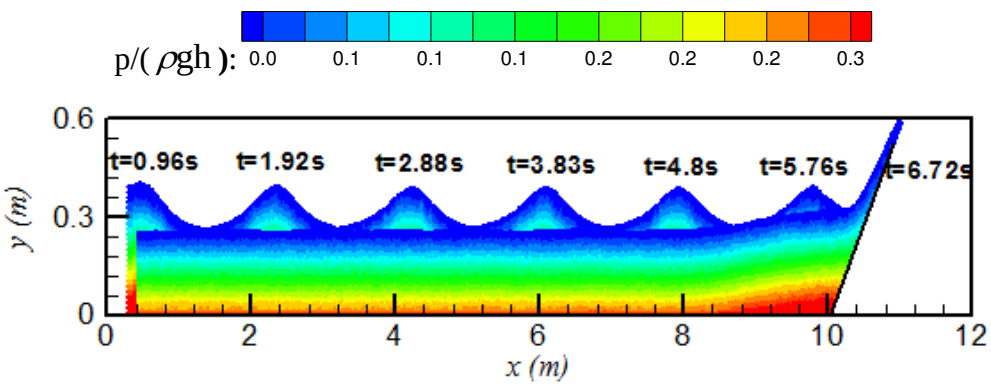


Fig. 14 Solitary wave profile and pressure contours during propagation and run-up.

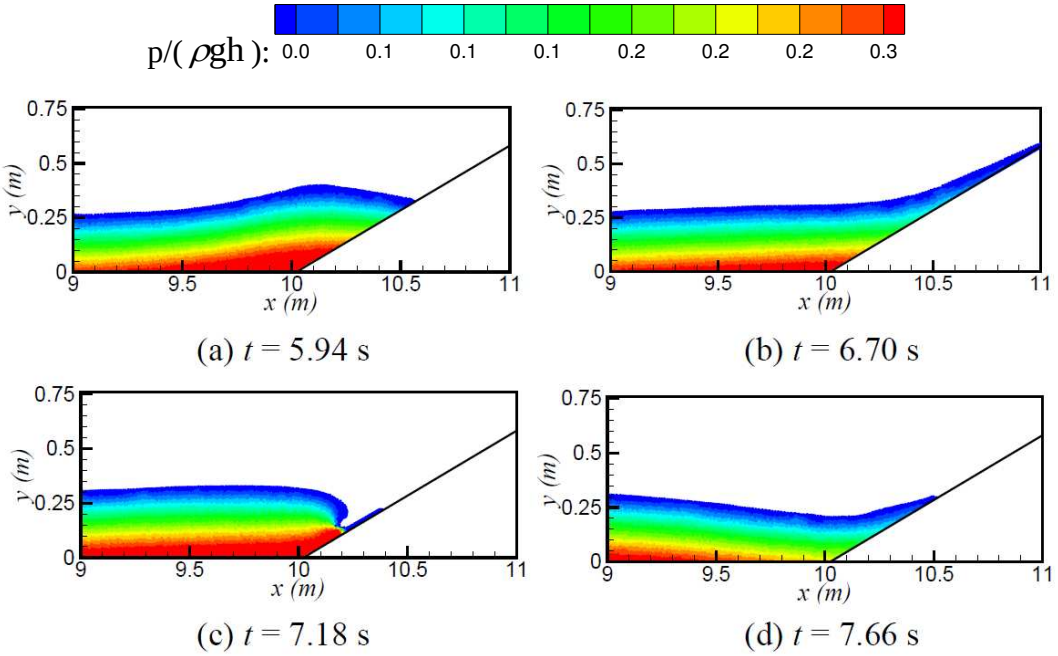


Fig. 15 Enlarged wave profile and pressure contours of coastal wave process: (a) run-up; (b) run-down; (c) over-turning; and (d) re run-up.

To quantitatively validate the wave impact pressures computed by CISPH3, Fig. 16 gives the comparisons of pressure time histories at sensor point $p_1$ with the experimental data. It shows that the maximum wave impact pressure computed by CISPH3 agrees quite well with the experimental value at time $t(g/h)^{1/2}$ = 18.5. However, during the solitary wave running-down and over-turning around $t(g/h)^{1/2}$ = 22.5, there exist severe pressure oscillations in the experimental data. Similar oscillations are also found in the CISPH3 numerical results, but the arrival time and amplitude of this oscillating pressure are reasonably predicted. It is also found that there is particle overshooting in the SPH results at this moment, which could be due to the lack of two-phase SPH modeling, in which the influence of air could adequately dampen the violent pressure oscillations. In general, we can see that the proposed CISPH3 method has well reproduced the entire experimental pressure history. Besides, to demonstrate the superiority of CISPH3 over the original and two other ISPH correction schemes, Fig. 16 includes the relevant numerical results as well. The enlarged figure shows that the original ISPH model predicted a later arrival of peak pressure although the pressure amplitude has been well predicted. On the other hand, both CISPH1 and CIPSH2 models predicted an early arrival and smaller peak pressure values.

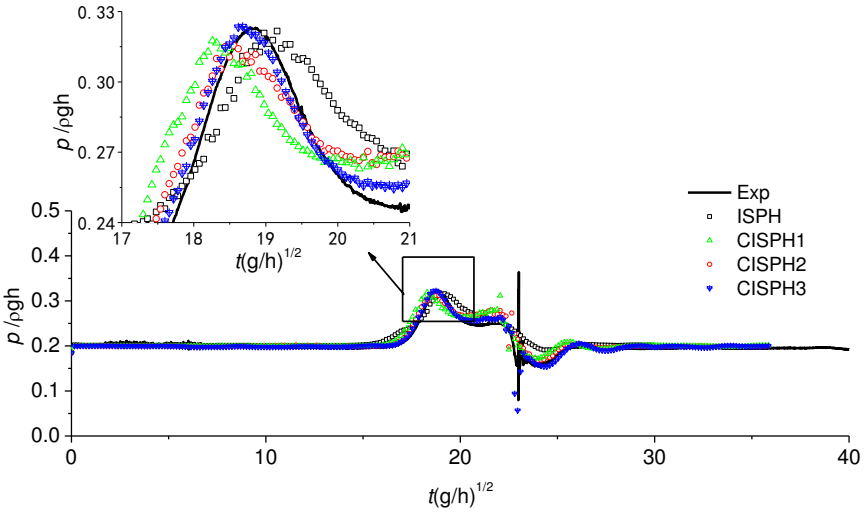


Fig. 16 Comparisons of time history of wave impact pressures between experimental data and different ISPH results.

6.2 Dam-break flow impact on a vertical wall

Dam-break flow and its impact against a vertical wall have been widely used as a benchmark test for the assessment of numerical models, and this is also used here for our CISPH3 pressure gradient algorithm. A rectangular column of water is contained in a tank. The initial column of water is 0.68 m wide and 0.12 m high, and the horizontal length of the tank is 1.18 m. The flows are allowed to move toward the right vertical wall. The schematic sketch of the dam-break domain is shown in Fig. 17. The numerical settings follow the physical experiment carried out by Hu and Kashiwagi (2004). Two sensor points $P_1$ and $P_2$ are located on the left and right walls, respectively, at a distance of 0.01 m from the tank bottom to record time history of the fluid pressures. In CISPH3 computations, we take the particle size dx = 0.0012 m and time step dt = 0.0003 s.

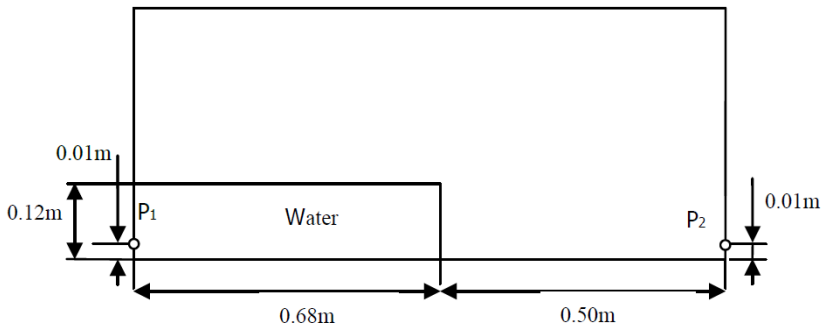


Fig. 17 Schematic view of dam-break flow impact on vertical wall (Hu and Kashiwagi, 2004).

Fig. 18 gives the snapshots of dam-break flow and pressure distributions at different times. The simulations clearly demonstrate the dam collapse process, with subsequent flood wave propagating, hitting on the right side of vertical wall, returning back and over-turning, generating flow jet and cavity region, etc. Many complex violent flow features have been adequately captured by our CISPH3 computations. One important phenomenon we have observed is that the left side wall is always located within the quasi-hydrostatic pressure region, where the flow situation is relatively quiet. In contrast, the right side wall experiences frequent dynamic impact pressures, due to the violent flow oscillations and interactions. Fig. 18 (c) gives an enlarged snapshot of the overturning wave, which is an indication that CISPH3 can accurately capture the complex free surface and provide the stable pressure distribution.

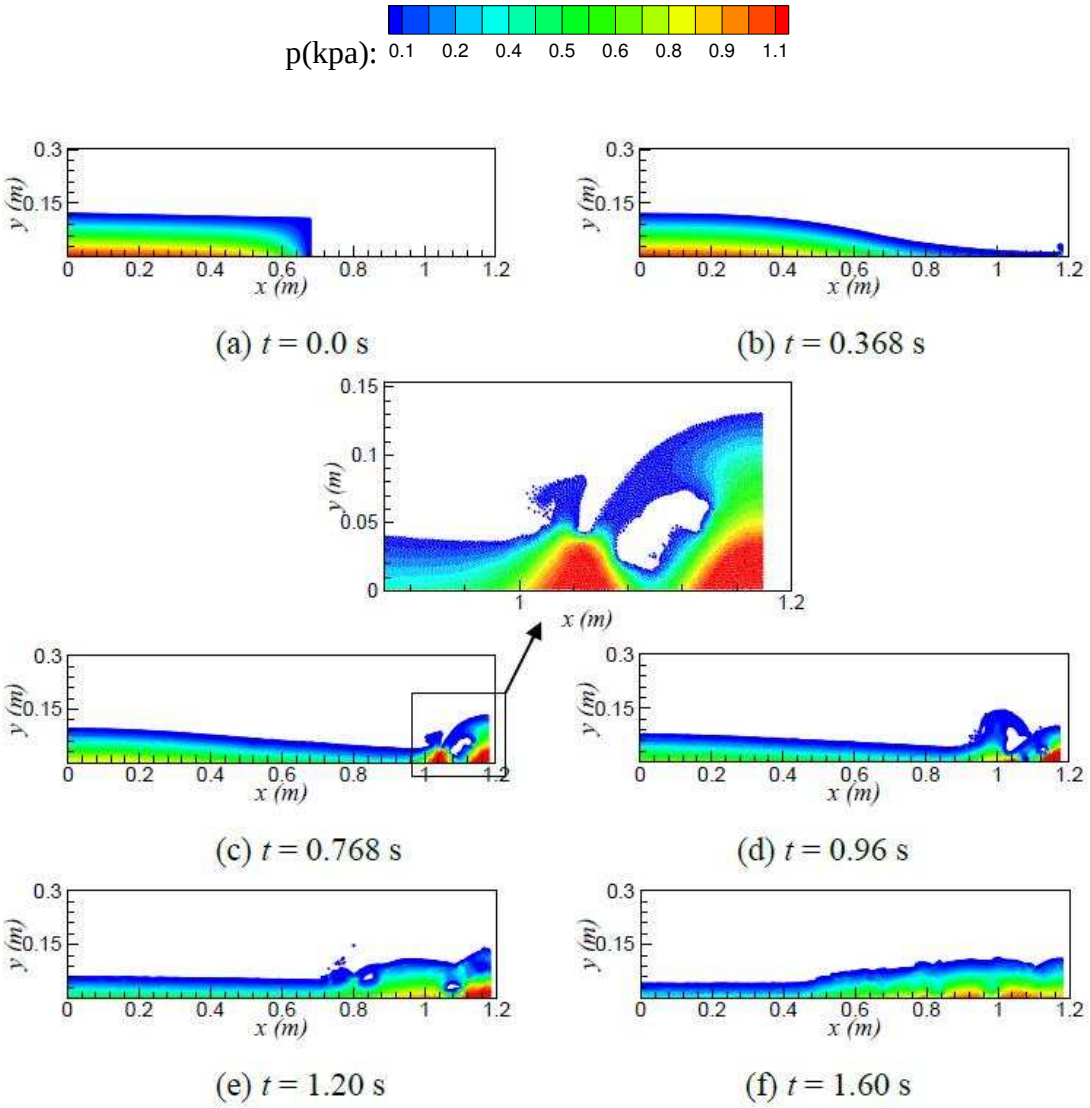


Fig. 18 Snapshots of dam-break flow with pressure contours at different times.

Fig. 19 gives the time history of pressures at two sensors on the left and right walls, $P_1$ and $P_2$, respectively. For both $P_1$ and $P_2$, different vertical locations are considered at a distance of 0.01 m, 0.02 m, 0.03 m, 0.04 m and 0.05 m from the reference level to make a comparison. According to the result shown in Fig. 19 (a), we could see that the pressure distributions at all $P_1$ locations follow nearly the hydrostatic pressure. This can be clearly seen from a cluster of the parallel pressure lines which are equally spaced and decrease with the retreat of free water surfaces. On the other hand, the pressure histories at all $P_2$ locations are rather complex as shown in Fig. 19 (b), in that wave impact pressures rise drastically and the maximum impact pressure is much larger than the hydrostatic pressure. Besides, the impact pressures at different vertical levels demonstrate different characteristics. For example, the impact pressure measured at y = 0.01 m indicates a clear double-peak pattern, while a single-peak feature has been observed at all the other locations. Also, the gaps between adjacent pressure lines are no longer uniform and this is more obvious during the first wave impact process.

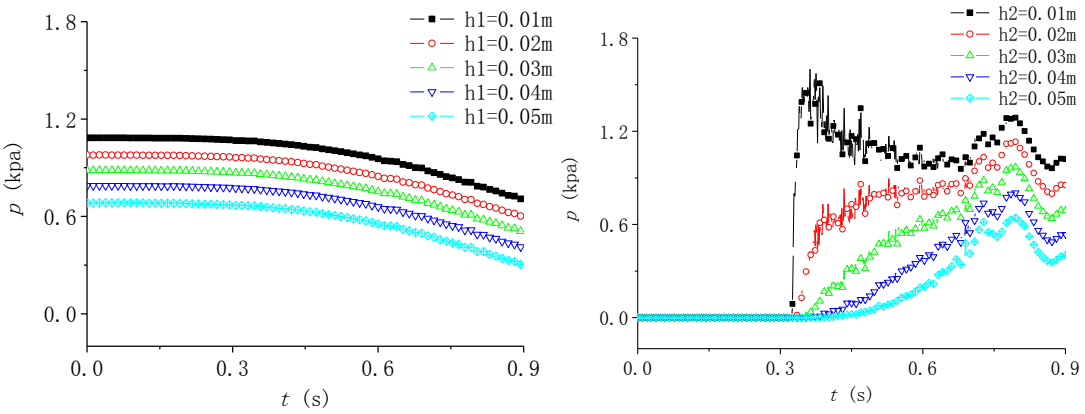


(a) Sensor $P_1$ (b) Sensor $P_2$

Fig. 19 Pressure time history at different sensor points of dam-break flow.

In order to quantify the accuracy of numerical model, Fig. 20 gives the comparison of pressure time histories between the experimental data (Hu and Kashiwagi, 2004) and CISPH3 results on sensor point $P_2$ at a distance of 0.01 m from the tank bottom. It shows that CISPH3 computations can accurately predict the first maximum impact pressure around time t = 0.36 s. Furthermore, it can also well capture the rise and magnitude of the second pressure peak, which was caused by the over-turning of wave during running-down. However, we should see that some kinds of oscillations exist in the pressure time history, due to the violent dam-break flow impact. It is also found out that the pressures are overestimated by the CISPH3 model after the second pressure peak. As recently reported by Gui et al. (2014), the lack of turbulence modeling could be one of the main reasons for this. They pointed out that the

turbulence modeling coupled with an ISPH solver could significantly improve over the non-turbulent modeling and reduce the pressure errors by about 50% for the same test case. In spite of these uncertainties, the general pressure evolution profile and peak pressure values, which are the two important reference parameters widely used in the practical design, have been satisfactorily predicted by the present CISPH3 model with the improved first-order pressure derivative scheme.

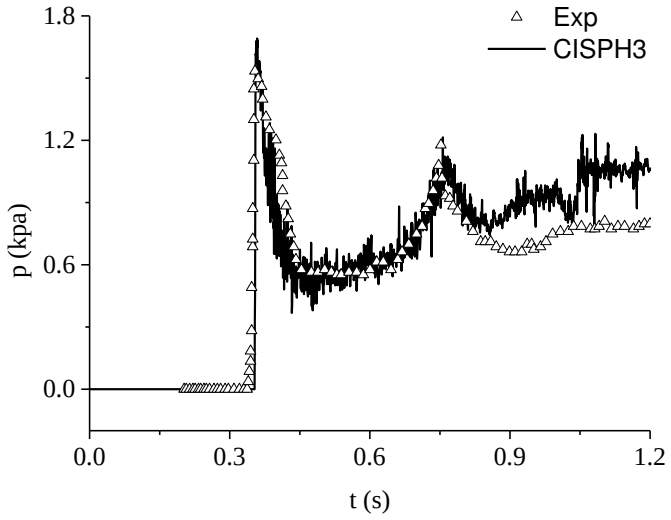


Fig. 20 Comparisons of time history of impact pressure between experimental data (Hu and Kashiwagi, 2004) and CISPH3 results.

6.3 Dam-break flow overtopping on a trapezoidal structure

The existence of downstream structure can significantly influence the complexity of dam-break flood wave during its propagation by changing the maximum flow depth, propagation velocity and flow regime, etc. Moreover, it can also cause the formation of negative waves that travel against the upstream direction (Pu et al., 2013). Here the proposed model is tested by using the experiment data of Ozmen-Cagatay and Kocaman (2011) for a dam-break flow over a trapezoidal obstacle. The 2-D sketch of the laboratory flume is shown in Fig. 21, which is 9 m long, 0.3 m wide and 0.34 m high. A plate (dam) is located 4.65 m from the upstream channel entrance. The initial water depth in the reservoir is 0.25 m and the downstream area is dry. A symmetrical trapezoidal shaped obstacle, which is 0.075 m high and 1.0 m base wide, is located 1.5 m downstream from the dam site. This case will be simulated by using the proposed CISPH3 model as shown in Eq. (29) and a particle size dx = 0.007 m and time step dt = 0.001 s are used. Similar spatial resolution was also used by Ozmen-Cagatay and Kocaman (2011) in their RANS and SWE computations.

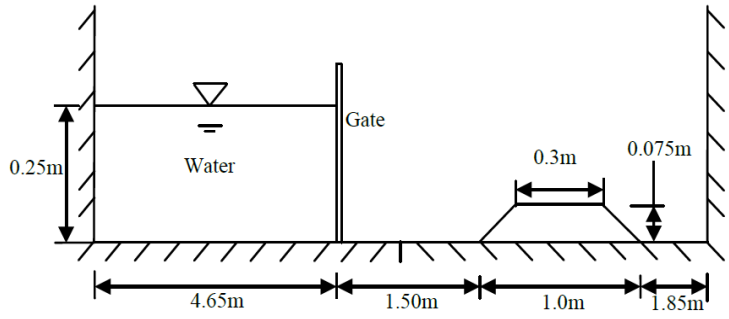


Fig. 21 Sketch of laboratory flume of dam-break flow over a trapezoidal structure.

Fig. 22 shows the snapshot of dam-break wave profiles and pressure distributions at different times computed by CISPH3. In general, the simulated flow patterns are very similar to those reported by Ozmen-Cagatay and Kocaman (2011) in their numerical simulations and laboratory experiments. It shows that after the dam breaks, very complex flow patterns developed due to the presence of the obstacle. In the dam area the pressures under the water surface are nearly hydrostatic, while the pressures near the interaction region between dam-break wave and trapezoidal structure demonstrate very strong dynamic behaviors. Fig. 22 also gives zoomed snapshot of free surface profiles near the trapezoidal structure. According to the comparison between experimental data and numerical results, CISPH3 is found to achieve very good agreement with the physical details, including both smooth and breaking free surfaces. It is shown that when the dam-break flood wave reaches the obstacle, part of the flow is reflected to form a negative bore travelling towards the upstream direction, while another part overtops over the structure crest and propagates in the downstream direction. Ozmen-Cagatay and Kocaman (2011) observed a spilling type wave breaker in the laboratory experiment but we found a plunging one in the present numerical simulations, which is consistent with their numerical RANS results.

Fig. 23 (a) – (f) shows the comparisons of computed free surface profiles with experimental data measured by Ozmen-Cagatay and Kocaman (2011), from t = 1.9 s to t = 6.7 s. It is shown that when the dam-break wave reaches the obstacle, the flow forms a hydraulic jump and overtops over the step at t = 1.9 s. Then the wave height continues to rise until t = 2.8 s, when the reflective negative wave starts to propagate upstream in the form of a bore. Throughout all the times shown in Fig. 23, the ISPH computed water surfaces are in very good agreement with the measured data along the whole channel region.

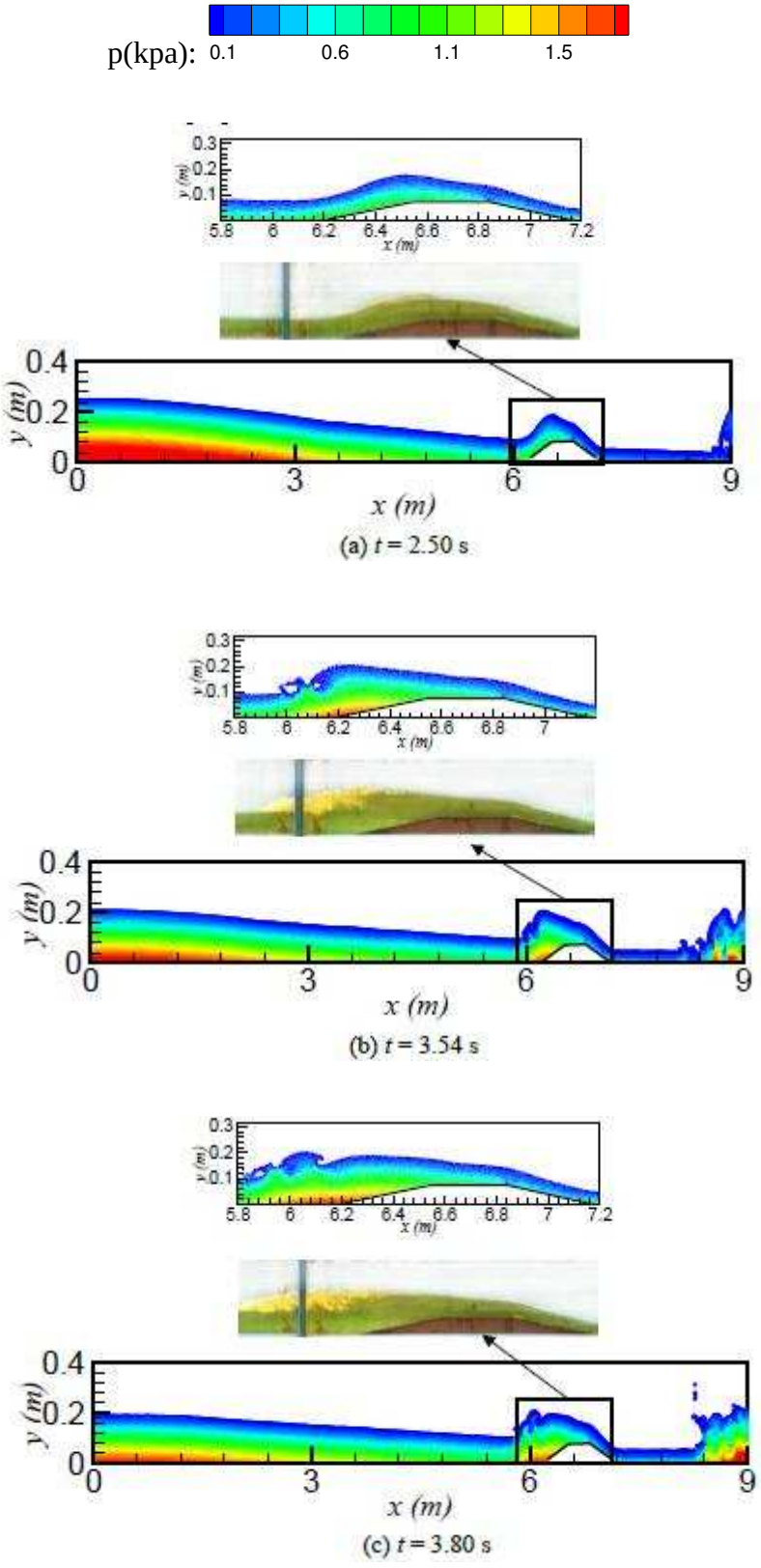


Fig. 22 Snapshots of dam-break flow profiles and pressure distributions at different times.

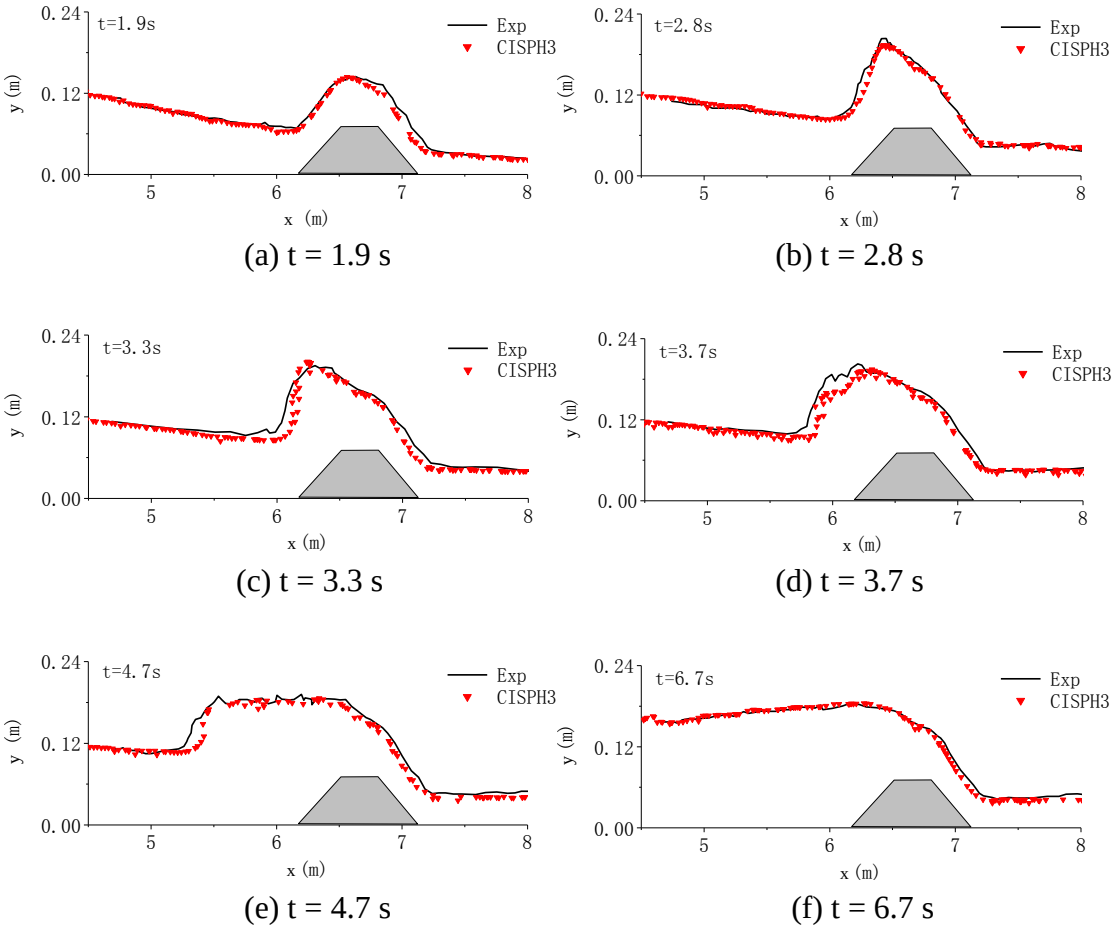


Fig. 23 Comparisons of water surface profiles between experimental data and CISPH3 results.

In the numerical simulations of Ozmen-Cagatay and Kocaman (2011), their SWE results demonstrated obvious deviations with the experimental data as compared with their RANS results. However, they found obvious errors in the reflected wave profile in RANS results at the early stage of negative wave generation (at t = 3.3 s and 3.7 s). They attributed this to the formation of plunging wave breaker in the computation while a spilling wave breaking was found in the laboratory experiment. They suggested different turbulence models should be tested to capture the plunging wave breaking. On the other hand, our proposed ISPH model can well reproduce the whole process of negative wave initiation, formation and propagation with very promising results. We may keep in mind that our CISPH3 used a slightly rough spatial resolution of dx = 0.007 m, compare with a grid size of 0.005 m used in the RANS model of Ozmen-Cagatay and Kocaman (2011). Also, no explicit turbulence model is coupled with the ISPH solver. The good performance could be due to that ISPH is a mesh-free particle modeling technique and thus it is equipped with unique advantages to deal with the large deformation of free surfaces and complex fluid-structure interactions.

Finally, to show the robustness of CISPH3 correction scheme over existing first-order derivative calculation models (i.e. original ISPH, CISPH1 and CISPH2), Fig. 24 (a) – (b) compares different numerical results based on the same particle resolution with the experimental data of Ozmen-Cagatay and Kocaman (2011). It shows that at the early stage of the dam-break flow, i.e. t = 1.9 s, almost the same profiles were obtained for the original and three corrected ISPH computations. However, as the simulations continue to the later stage of flow-structure interactions at t = 6.7 s, the differences among different ISPH methods become more obvious. Again the proposed CISPH3 correction model seems to perform the most satisfactorily in this case as well.

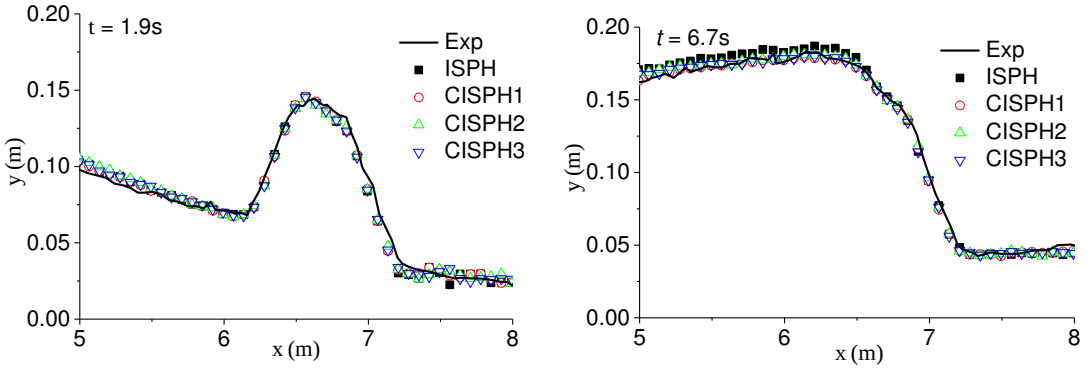


(a) t = 1.9 s (b) t = 6.7 s

Fig. 24 Comparisons of water surface profiles between experimental data and different ISPH results at early and later stages of dam-break flow.

## 7. Conclusions

The paper reviewed four different first-order derivative schemes of pressure, which is essential in the mesh-free SPH modelling techniques. The recommended formulation of CISPH3 uses a simple FDM representation based on the Taylor series expansion and leads to a satisfactory improvement in the wave impact predictions. By using the benchmark patch test, solitary wave propagation over a constant depth and standing wave generation, it has been found that CISPH3 correction scheme improved the ISPH accuracy by achieving either higher convergence rate or less numerical error. As practical model application, CISPH3 is further used in three engineering scenarios, including solitary wave impact on a slope, dam-break flow impact on a vertical wall and overtopping on a structure. The computed free surface profiles and hydrodynamic impact pressures have been found to agree well with the experimental data.

Essentially the simplified FDM scheme used in CISPH3 was derived from the Taylor series by ignoring the terms of second and higher order derivatives and is therefore second-order accurate. Numerical tests in Ma (2008) have demonstrated that it is as accurate as the MLS or even more under certain circumstances. It could also be efficiently used in other mesh-free methods especially when the particles are highly irregularly distributed, i.e. under wave breaking or wave impact. In spite that SFDM was originally developed for the MLPG_R method (Ma, 2008), we would think it can also be adopted for the interpolation of a function and calculation of its gradient in other mesh-less methods as well, such as general SPH field. This is partially supported by the fact that a sensitivity test with different $\gamma$ coefficient in Eq. (12) (i.e. 0.05 other than 0.01) on the solitary wave propagation case showed CISPH3 still performed much better than the other three calculation models.

However, we should note that a better prediction of wave impact pressures actually relies on the accurate modeling of a variety of influence factors such as the air entrainment, two-phase flow, turbulence and compressibility of air bubbles.

## Acknowledgements

This research work is supported by the National Natural Science Foundation of China (Nos. 51009034, 51279041, 51479087).

## References

Atluri, S. N. and Shen, S. (2002), The meshless local Petrov–Galerkin (MLPG) method: a simple and less-costly alternative to the finite element and boundary element methods, Computational Modelling in Engineering & Sciences, 3(1), 11-52.

Bonet, J. and Lok, T. S. L. (1999), Variational and momentum preservation aspects of smooth particle hydrodynamics formulations, Computer Method in Applied Mechanics & Engineering, 180, 97-115.

Colagrossi, A. and Landrini, M. (2003), Numerical simulation of interfacial flows by smoothed particle hydrodynamics, Journal of Computational Physics, 191, 448–475.

Crespo, A. J. C., Gomez-Gesteira, M. and Dalrymple, R. A. (2007), 3D SPH simulation of large waves mitigation with a dike, Journal of Hydraulic Research, 45(5), 631-642.

Fatehi, R. and Manzari, M. T. (2011), Error estimation in smoothed particle hydrodynamics and a new scheme for second derivatives, Computers & Mathematics with Applications, 61, 482-498.

Gomez-Gesteira, M., Cerqueiro, D., Crespo, C. and Dalrymple, R. A. (2005), Green water overtopping analyzed with a SPH model, Ocean Engineering, 32, 223–238.

Gui, Q., Shao, S. and Dong, P. (2014), Wave impact simulations by an improved ISPH model, Journal of Waterway, Port, Coastal and Ocean, 140(3), 04014005.

Hu, C. H. and Kashiwagi, M. (2004), A CIP method for numerical simulations of violent free surface flows, Journal of Marine Science and Technology, 9 (4), 143-157.

Hu, X. Y. and Adams, N. A. (2007), An incompressible multi-phase SPH method, Journal of Computational Physics, 227, 264-278.

Jian, W., Liang, D. and Shao, S. (2011), Simulation of solitary wave impact on coastal structures using weakly compressible and incompressible SPH methods, Proceedings of the 21st International Offshore and Polar Engineering Conference, Hawaii, USA, June 19-24, 711-717.

Jian, W., Liang, D., Shao, S., Chen, R. and Yang, K. (2016), Smoothed particle hydrodynamics simulations of dam-break flows around movable structures, International Journal of Offshore and Polar Engineering, 26(1), 33-40.

Khayyer, A., Gotoh, H. and Shao, S. (2008), Corrected incompressible SPH method for accurate water-surface tracking in breaking waves, Coastal Engineering, 55(3), 236-250.

Khayyer, A. and Gotoh, H. (2011), Enhancement of stability and accuracy of the moving particle semi-implicit method, Journal of Computational Physics, 230(2011), 3093-3118.

Lind, S. J., Xu, R., Stansby, P. K. and Rogers, B. D. (2012), Incompressible smoothed particle hydrodynamics for free-surface flows: A generalised diffusion-based algorithm for stability and validations for impulsive flows and propagating waves, Journal of Computational Physics, 231(4), 1499-1523.

Liu, W. K., Jun, S. and Zhang, Y. (1995), Reproducing kernel particle methods, International Journal for Numerical Method in Fluids, 20, 1081-1106.

Lucy, L. B. (1977), A numerical approach to the testing of the fission hypothesis, The Astronomical Journal, 82(12), 1013 -1024.

Ma, Q. W. (2005), Meshless local Petrov–Galerkin method for two-dimensional nonlinear water wave problems, Journal of Computational Physics, 205, 611–625.

Ma, Q. W. (2008), A new meshless interpolation scheme for MLPG_R method, Computer Modeling in Engineering & Sciences, 23(2), 75-89.

Ma, Q. W. and Zhou, J. T. (2009), MLPG_R method for numerical simulation of 2D breaking waves, Computer Modeling in Engineering & Sciences, 43(3), 277-303.

Monaghan, J. J. (1994), Simulating free surface flows with SPH, Journal of Computational Physics, 110, 399-406.

Oger, G., Doring, M., Alessandrini, B. and Ferrant, P. (2007), An improved SPH method: towards higher order convergence, Journal of Computational Physics, 225, 1472-1492.

Ozmen-Cagatay, H. and Kocaman, S. (2011), Dam-break flow in the presence of obstacle: experiment and CFD simulation, Engineering Applications of Computational Fluid Mechanics, 5(4), 541-552.

Pu, J. H., Shao, S., Huang, Y. and Hussain, K. (2013), Evaluations of SWEs and SPH numerical modeling techniques for dam break flows, Engineering Applications of Computational Fluid Mechanics, 7(4), 544-563.

Schwaiger, H. F. (2008), An implicit corrected SPH formulation for thermal diffusion with linear free surface boundary conditions, International Journal for Numerical Methods in Engineering, 75, 647–671.

Souto-Iglesias, A., Delorme, L., Pérez-Rojas, L. and Abril-Perez, S. (2006), Liquid moment amplitude assessment in sloshing type problems with smooth particle hydrodynamics, Ocean Engineering, 33(11), 1462-1484.

Violeau, D. and Rogers, B. D. (2016), Smoothed particle hydrodynamics (SPH) for free-surface flows: past, present and future, Journal of Hydraulic Research, 54(1), 1-26.

Xu, R., Stansby, P. and Laurence, D. (2009), Accuracy and stability in incompressible SPH (ISPH) based on the projection method and a new approach, Journal of Computational Physics, 228, 6703–6725.

Xu, X. Y. and Deng, X. L. (2016), An improved weakly compressible SPH method for simulating free surface flows of viscous and viscoelastic fluids, Computer Physics Communications, 201, 43-62.

Zhang, G. M. and Batra, R. C. (2009), Symmetric smoothed particle hydrodynamics (SSPH) method and its application to elastic problems, Computational Mechanics, 43(3), 321-340.

Zhang, S., Morita, K., Fukuda, K. and Shirakawa, N. (2006), An improved MPS method for numerical simulations of convective heat transfer problems, International Journal for Numerical Methods in Fluids, 51(1), 31-47.

Zheng, X., Ma, Q. W. and Duan, W. Y. (2014), Incompressible SPH method based on Rankine source solution for violent water wave simulation, Journal of Computational Physics, 276, 291-314.

Zou, Z. L. (2005), Water Wave Theories and Their Applications, Science Press, Beijing (in Chinese).